31th Symposium on Naval Hydrodynamics
Monterey, California, 11-16 September 2016

Feature-Resolved Simulations of Turbulence over Superhydrophobic Surfaces

Yixuan Li, Karim Alame and Krishnan Mahesh
(University of Minnesota, USA)

ABSTRACT

Direct numerical simulations are used to study the drag reduction effect of superhydrophobic surfaces in both laminar and turbulent regimes. The superhydrophobic surfaces are longitudinal grooves mounted on one side of a plane channel. The laminar simulations are compared to the experiments of Maynes et al. (2007). The effects of groove geometry, trapped gas and interface meniscus are independently studied. An alternative to the commonly used zero-shear boundary condition is applied to consider the effect of the gas at the interface. Fully wetted turbulent simulations were performed at $Re_\tau = \frac{\delta}{\delta_\nu} = 400$ with groove width $w^+ = w/\delta_\nu = 3.6$ and height $h^+ = h/\delta_\nu = 3.6$ in viscous wall unit. The results show that geometry causes an apparent slip to the external flow which extends up to $y^+ = y/\delta_\nu = 2$ from the wall and yields overall drag reduction of about 5%. The instantaneous solution shows behavior similar to riblets in that the near wall vorticity does not penetrate into the grooves yielding overall drag reduction. The failure of the interface is examined and a simple criterion is proposed.

INTRODUCTION

Superhydrophobic surfaces (SHS) have drawn much attention for their potential in viscous friction reduction. The effects of SHS are attributed to surface chemistry and roughness. In both static and dynamic regimes, the grooves reduce contact area since a lower viscosity fluid is trapped inside the groove and is in contact with the solid. This regime is known as the Cassie-Baxter regime (Cassie and Baxter, 1944). It is not fully understood if the Cassie-Baxter regime can be sustained in the presence of high shear rates and flow unsteadiness in the turbulent boundary layer. Also, most past studies have been performed for laminar flow in micro channels (see Rothstein (2010)) and the gas-liquid interface is treated as a zero-shear interface (Philip, 1972a,b). Curvature effects were investigated and analytical solutions were proposed for slip lengths ($b = u_{\text{slip}}/(\partial u/\partial y)$) as a function of curvature and gap span for zero-shear interfaces (Teo and Khoo, 2010). The impact of curvature on the cross-sectional area was quantified using small perturbation theory (Sbragaglia and Prosperetti, 2007) and the results are consistent with the scaling law proposed by Ybert et al. (2007). Experimentally, direct measurements of slip velocities have been performed (e.g. Pit et al. (1999), Tretheway and Meinhart (2002, 2004)).

Busse and Sandham (2012) performed a parametric study of the streamwise and spanwise slip lengths, and related the slip lengths to the change of drag using DNS at $Re_\tau = 180$ and $Re_\tau = 360$. Park et al. (2013) simulated the SHS as a patterned slip and no-shear boundary conditions on both walls of the turbulent channel up to $Re_\tau = 590$, and examined the dependence of the effective slip length on Reynolds number. The wall pressure fluctuations were studied by Seo et al. (2015) at $Re_\tau = 200$.

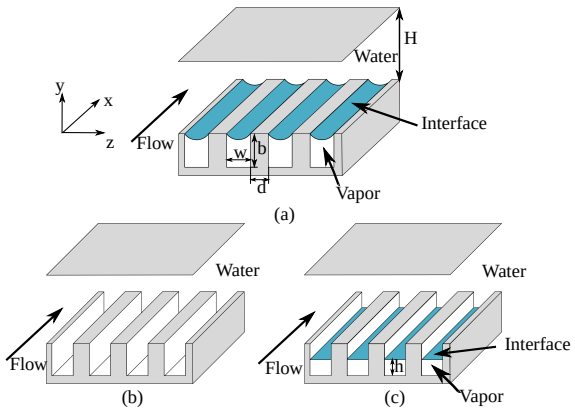

Figure 1: The channel geometry and groove configuration.

In this paper, we study the microphysics of drag reduction in SHS with longitudinal grooves in laminar and turbulent regimes. We use direct numerical simulation

to resolve the flow inside the grooves. We study the effect of geometry by performing fully wetted simulations, and the effect of gas by capturing the coupled interaction between the liquid and gas phases. Figure 1 shows a schematic of the problem investigated.

NUMERICAL METHOD

Direct Numerical Simulation (DNS) using the Volume-of-Fluid (VOF) methodology is used to study the liquid-gas interface within a groove. The scalar transport equation which governs the color function c is given by:

$$\frac{\partial c}{\partial t} + u_j \frac{\partial c}{\partial x_j} = 0 \tag{1}$$

The VOF methodology is based on reconstruction and advection steps. The reconstruction step geometrically conserves the volume in each cell and therefore conserves mass. The advection step prevents over- and under-shoots in the value of the color function, which ensures boundedness. The DNS is performed using the finite volume algorithm developed by Mahesh et al. (2004) for solving the incompressible Navier-Stokes equations on unstructured grids. The governing equations are given by the momentum and continuity equations:

$$\frac{\partial u_i}{\partial t} + \frac{\partial}{\partial x_j}(u_i u_j) = -\frac{1}{\rho}\frac{\partial p}{\partial x_i} + \frac{1}{\rho}\frac{\partial}{\partial x_j}\left[\mu\left(\frac{\partial u_i}{\partial x_j} + \frac{\partial u_j}{\partial x_i}\right)\right] + F_{st} + F_b \tag{2}$$

$$\frac{\partial u_i}{\partial x_i} = 0, \tag{3}$$

where the index notation i of x_i denotes the streamwise (x), wall-normal (y), and spanwise (z) directions. The velocity notation u_i denote the components of the velocity vector in x, y, z directions, p is the pressure, ρ is the density and μ is the viscosity of the fluid, and F_b is the body force. For the multiphase simulation, F_{st} is the surface tension force modeled as a source term and is given by the continuum surface force:

$$F_{st} = \sigma \kappa \nabla c. \tag{4}$$

Here σ is the surface tension constant, κ is the curvature of the interface calculated using the height function and ∇c is the gradient of the color function that is equivalent to the surface normals. The fluids are assumed to be immiscible hence the density(ρ_1 and ρ_2) and viscosity(μ_1 and μ_2) in each phase are taken as a constant and evaluated as follows:

$$\rho = \rho_1 + (\rho_2 - \rho_1)c \tag{5}$$

$$\mu = \mu_1 + (\mu_2 - \mu_1)c \tag{6}$$

Different configurations were studied within the laminar regime and are listed in table 1. In the turbulent regime, DNS is performed of a feature-resolved fully wetted channel with micro-grooves on the bottom surface. $Re_\tau = 400$, the groove width $w^+ = 3.6$ and height $h^+ = 3.6$. The introduction of micro-grooves makes the flow statistically inhomogeneous in the spanwise direction. Therefore, the statistics are averaged temporally and spatially in the streamwise direction, and ensemble-averaged over all the grooves.

RESULTS

Comparison to Experiment

Maynes et al. (2007) conducted an experiment with grooves on the top and bottom wall for a laminar channel. The grooves were closed off at the end, inducing a reverse flow in the gas pockets. Drag reduction is quantified as a function of ϕ, using the product fRe, where $\phi = w/(w+d)$ is the non-dimensional groove width, w and d are the width of the groove and the distance between the grooves respectively, f is the Darcy friction factor and Re is the Reynolds number.

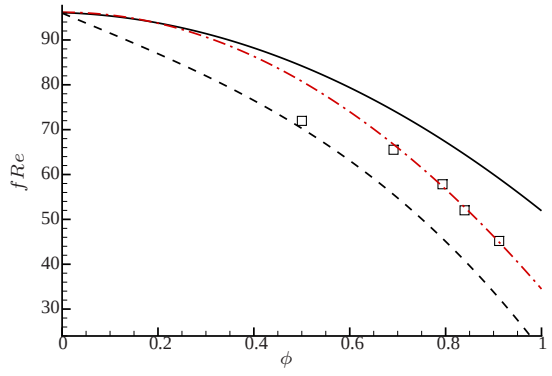

Figure 2: Comparison between the VOF results and experiment. The dashed line is for gas pocket filling the entire groove, the red dash-dot line represents a 20% fluid penetration into the groove, and the solid line is for a fully wetted case (100% fluid penetration). Symbols represent the experiment.

VOF simulations of the Maynes et al. (2007) experiments were performed allowing for reverse flow in the gas pocket. The penetration of the liquid into the groove was varied; figure 2 shows our results compared to the experiment. Here the dashed line is for gas pocket filling

the entire groove, the red dash-dot line represents 20% fluid penetration into the groove, and the solid line is for a fully wetted case (100% fluid penetration). Based on the comparison with experiment (symbols) it is clear that fluid penetrating the groove increases drag. In order to model this, a boundary condition should include geometric effects, amount of fluid penetrating the groove and the meniscus shape.

Laminar Channel

We discuss the role of the geometry, the shear stress on the interface, and the shape of the interface, see figure 1 for geometric parameters and flow configuration. H and W are the height and width of the channel respectively, b is the depth of the groove, and h is the height of the interface. First, the geometric effect is studied independently by modeling the fully wetted grooves (figure 1(b)). Second, the interface is assumed to be flat and the shear rate on the interface is modeled using the approximate boundary condition:

$$\frac{\mathrm{d}u_{\mathrm{liquid}}}{\mathrm{d}y} = \mu_r \frac{u_{\mathrm{liquid}}}{h} \tag{7}$$

where μ_r is defined as the ratio of the gas to liquid viscosity μ_{gas}/μ_{liquid}. Finally, the shape of the interface is taken into account by defining the meniscus using the Young-Laplace equation with prescribed pressure difference that sustains the curvature:

$$\Delta p = \sigma \nabla \cdot n \tag{8}$$

where Δp is the pressure difference, σ is the liquid-gas surface tension and n is the interface normal. We compare the VOF simulations with the Young-Laplace equation by varying the contact angle (defined in figure 3(a))as a boundary condition, and computing the pressure difference as a function of contact angle (figure 3(b)). The good agreement between the VOF simulations and the Young-Laplace equation shows that the Young-Laplace solution is a valid model.

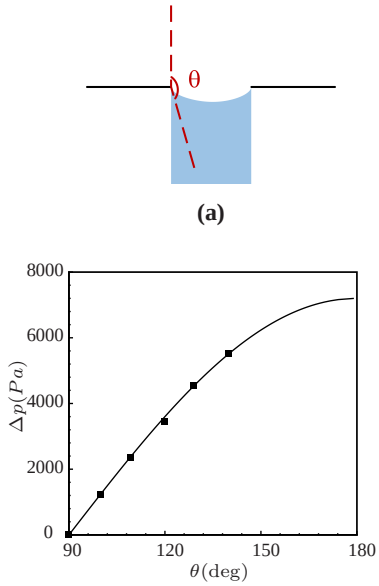

Figure 3: (a)Schematic of contact angle θ. (b)The contact angle of the meniscus in terms of the pressure difference. The solid line is derived from the Young-Laplace equation. The symbols are measured from VOF simulations.

Table 1 lists the simulations performed in the laminar regime. The SHS channels are simulated with a various combination of channel heights, groove and gas pocket sizes. Cases F7, F12 and F25 are simulations of fully wetted grooves; cases I7, I12 and I25 represent flat interface simulations; cases M7, M12 and M25 are meniscus simulations. $\phi = w/(w+d)$ is the coverage ratio of the grooves.

Table 1: Simulation parameters. The width of the channel is fixed at $W = 4$. The depth of the groove is $b = 2.5$.

Case	H	ϕ	h	Δp(kPa)
F7	7.52	1/4, 1/2, 3/4	n/a	n/a
F12	12.75	1/4, 1/2, 3/4	n/a	n/a
F25	25.0	1/4, 1/2, 3/4	n/a	n/a
I7	7.52	1/4, 1/2, 3/4	0.7, 1.5, 2.25, 2.5	n/a
I12	12.75	1/4, 1/2, 3/4	0.7, 1.5, 2.25, 2.5	n/a
I25	25.0	1/4, 1/2, 3/4	0.7, 1.5, 2.25, 2.5	n/a
M7	7.52	1/2	n/a	0, 1, 3, 6
M12	12.75	1/2	n/a	0, 1, 3, 6
M25	25.0	1/2	n/a	0, 1, 3, 6

All the laminar channel flow simulations are performed with constant flow rate. The drag reduction is defined as:

$$\mathrm{DR} = \frac{K_{\mathrm{no-slip}} - K_{\mathrm{SHS}}}{K_{\mathrm{no-slip}}}, \tag{9}$$

where K_{SHS} and $K_{\mathrm{no-slip}}$ are the body forces driving the SHS/no-slip channel flow for the same volume flow rate. The effective slip length and slip velocity are functions of the volume flow rate Q and are defined as follows:

$$\mathrm{b_{eff}} = -\frac{12\frac{QH}{W} - 1}{12\frac{QH}{W} - 4}, \tag{10}$$

$$u_{\mathrm{eff}} = \frac{2QH}{W} - \frac{1}{6}. \tag{11}$$

Here all lengths are normalized by the channel height H. The velocities are normalized by KH^2/μ. Figure 5 shows the drag reduction results. For a fixed groove geometry and gas pocket penetration, the drag reduction increases as the coverage ratio ϕ increases. For a fixed coverage ratio and groove geometry, the drag reduction increases as the amount of vapor in the groove increases. Note that even though low, fully wetted simulations show a drag reduction effect when the volume flow rate Q is measured in the channel part above the grooves. This is due to the fact that the liquid experiences slip over the liquid inside the grooves. The meniscal interface yields drag reduction that slightly exceeds the zero-shear planar interface prediction. Intriguingly, drag reduction of the SHS with meniscus shapes shows the highest drag reduction when Δp = 5kPa, then it drops down when Δp increases to 6kPa (see figure 4 for the trend of drag reduction against increasing θ or Δp). Good agreement is found between the VOF calculations and the calculations with the approximate boundary condition. This can be explained as a tradeoff between the local gas height and the arc length of the meniscus.

A similar trend is obtained for effective slip lengths and velocities (figure 6, 7). Also note that the simulations with modeled interface agree well with VOF simulations.

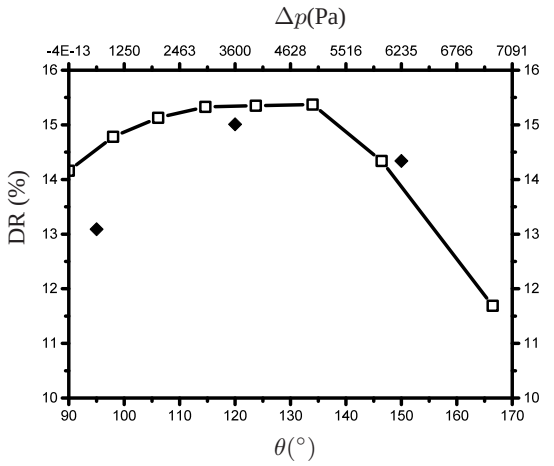

Figure 4: Variation of drag reduction with contact angle θ and pressure difference Δp. (Open symbols are approximate BC with meniscus shape simulations; solid symbols are VOF simulations).

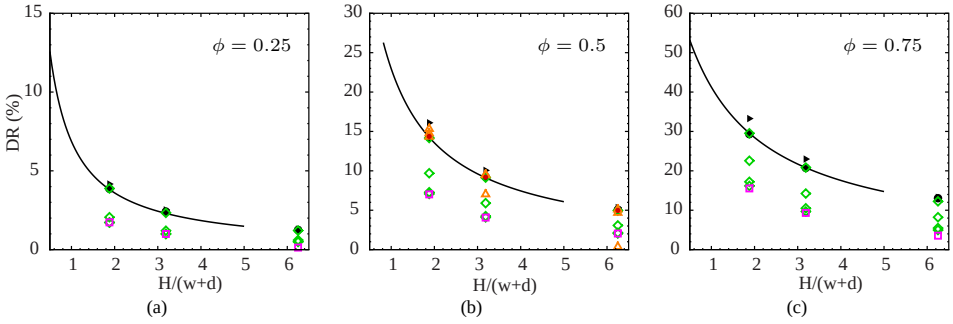

Figure 5: Drag reduction for all simulations. □ are for cases F7, F12, F25. ♢ are cases I7, I12, I25. Δ are cases M7, M12, M25. ► are VOF with equal pressure gradient in both phases. • are VOF with zero mass flow rate in groove. Solid line is Philip (1972a) theoretical prediction.

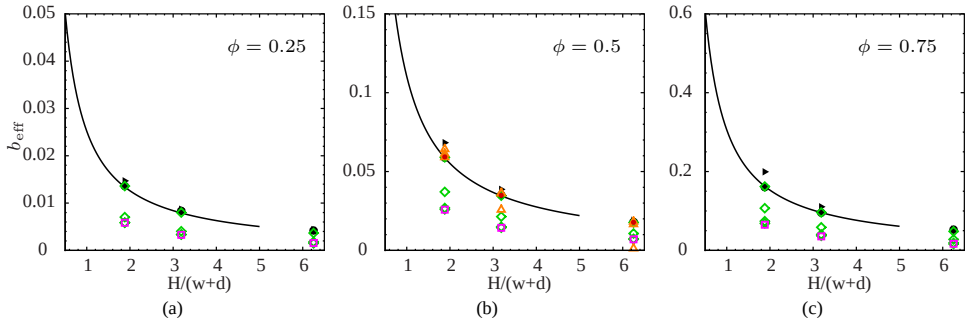

Figure 6: Effective slip length in different models. Symbols are the same as figure 5.

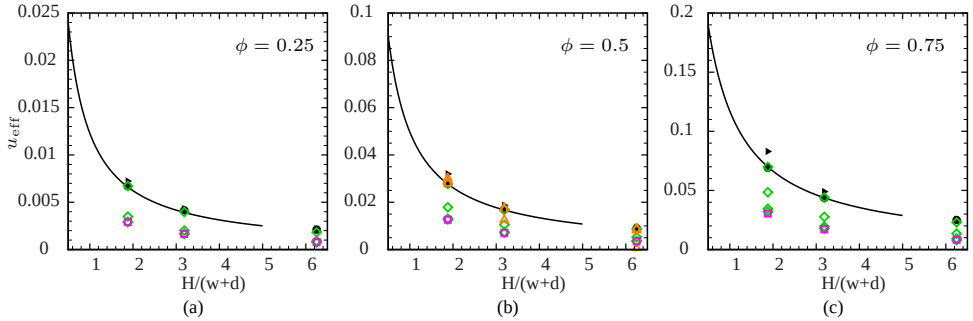

Figure 7: Effective slip velocity in different models. Symbols are the same as figure 5.

Table 2: Channel dimensions and spatial resolution of DNS.

	$(w+d)^+$	h^+	ϕ	L	W	Δx^+	Δy^+_{min}	Δy^+_c	Δz^+_{min}
Flat channel	–	–	–	$2\pi\delta$	$\pi\delta$	7.9	0.8	6.1	3.2
Grooved channel	4.11	3.6	0.875	6.58δ	3.29δ	10.3	0.4	6.0	0.257

Turbulent channel

First, DNS of a plane channel with smooth walls was performed and validated against Moser et al. (1999) at $Re_\tau = 395$ (figure 8); good agreement is observed. Table 2 lists the dimensions of the channel and grooves along with the spatial resolution. Note that the simulation resolves 320 grooves whose width w^+ and height h^+ are both 3.6. The cross section of each groove has 15 points in each direction. The grooves are assumed to be fully wetted to examine the effect of groove geometry independently.

Figure 9 shows contours of the streamwise velocity in a cross-sectional plane and a plane parallel to the bottom wall. Note that the grooves are barely visible on the outer scale; a close-up view shows low momentum fluid swirling within the grooves. Statistics are collected by averaging over time and the streamwise direction. Note that the flow is statistically inhomogeneous over the spanwise extent of a single groove. The inhomogeneous statistics are ensemble-averaged over each of the 320 grooves. Figure 10 shows profiles of mean velocity and turbulence intensities over the bottom half of the channel. Note that the grooves introduce an apparent slip to the mean velocity, whose magnitude decreases from the center of the groove towards the groove boundaries. The maximum value of slip is approximately $1.2u_\tau$. The effect of the grooves is felt over approximately 10 wall units, while the spanwise inhomogeneity due to the grooves extends to approximately 2 wall units (figure 11). The overall discharge increases by 5%.

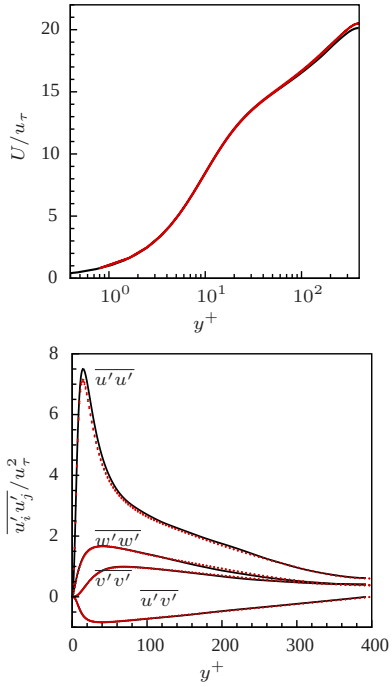

Figure 8: DNS statistics of the turbulent channel at $Re_\tau = 400$ (dotted line) compared with Moser et al. (1999) (solid line) benchmark data.

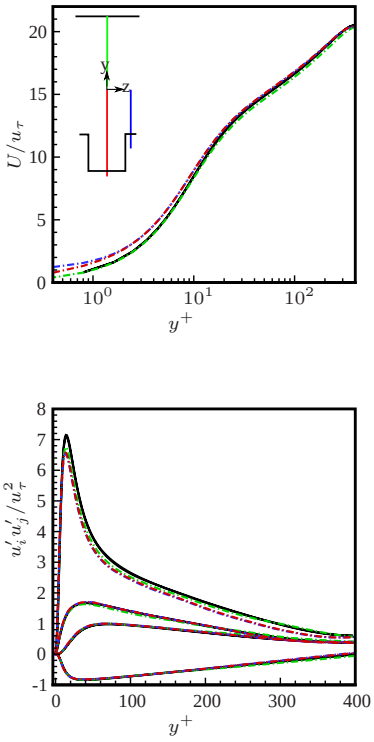

Figure 10: Conditional averaged (a) velocity and (b) intensities plots. Solid line represents smooth channel data; green line is the statistics of the top half channel (no grooves on top wall); red line is the statistics from the groove ridge to the channel center; blue line is the statistics from the groove center to the channel center, as is indicated in the figure inside (a) (For illustration purpose, the groove aspect ratio is different from the simulation).

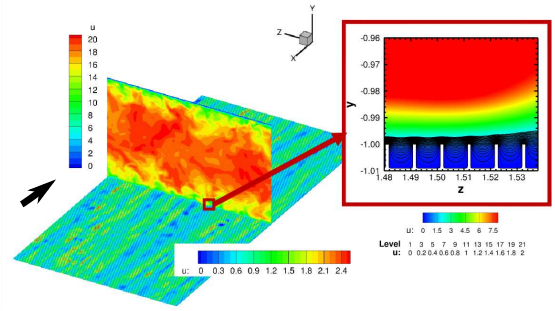

Figure 9: Instantaneous contours of streamwise velocity of the turbulent grooved channel. The arrow indicates the flow direction. In the 3D plot on the left, the increments of the contours of $y-z$ plane and $x-z$ plane are $2u_\tau$ and $0.3u_\tau$. Inside the red rectangle, it is the contour of streamwise velocity in the vicinity of 5 grooves. The increment of the color-filled contour plot is $1.5u_\tau$. The level of the line plot is $0.2u_\tau$.

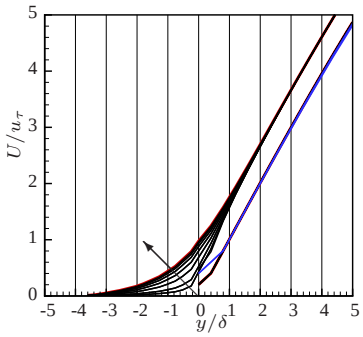

Figure 11: Zoomed-in view of the conditional averaged velocity profile. Black lines are extracted from difference phases of the groove, the arrow indicates the direction from the groove ridge to the groove center.

If the grooved surface is considered to be a rough surface, the roughness scale $s = 0.009$, which is compa-

rable to the viscous scale $\delta_\nu = 0.0025$. Assuming (Pope, 2000):

$$\frac{\mathrm{d}U}{\mathrm{d}y} = \frac{u_\tau}{y}\Phi\left(\frac{y}{\delta_\nu}, \frac{s}{\delta_\nu}\right), \tag{12}$$

the mean velocity in the log layer:

$$u^+ = \frac{1}{\kappa}\ln\left(\frac{y}{s}\right) + \tilde{B}\left(\frac{s}{\delta_\nu}\right). \tag{13}$$

Figure 11 shows that the velocity profiles converge beyond $y^+ \approx 2$ and are shifted by 0.8. Therefore,

$$\tilde{B} = B + 0.8, \tag{14}$$

where B is the constant in the log law.

The grooves affect the near wall turbulence in a manner similar to riblets (Choi et al., 1993). Figure 12 shows instantaneous contours of the vorticity field. Note that the spanwise extent of the near wall vorticity exceeds the groove width. The vortical fluctuations do not therefore penetrate into the grooves, yielding overall drag reduction.

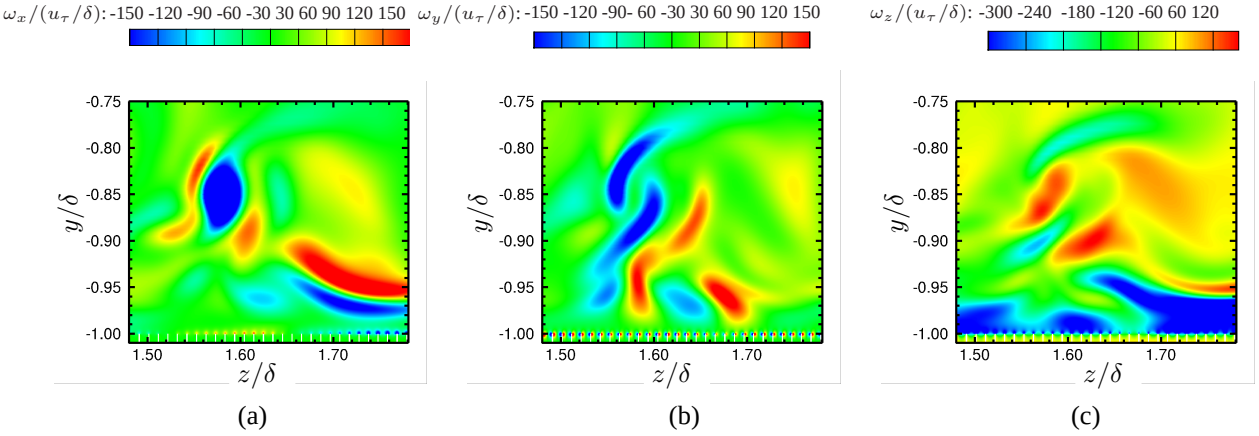

Figure 12: Instantaneous plots of the vorticity field (a) ω_x, (b) ω_y, (c) ω_z.

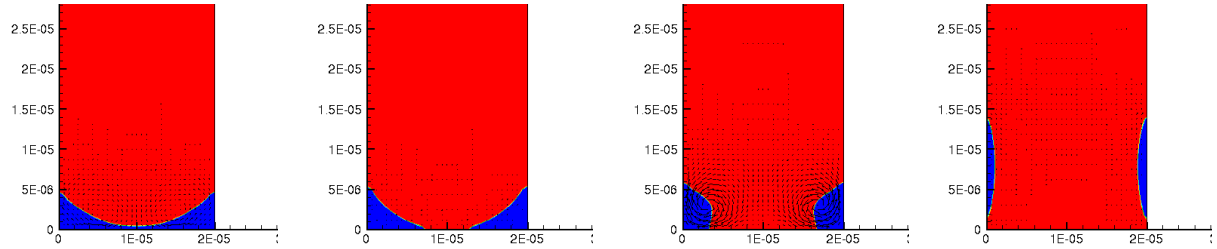

Figure 13: A time sequence images depicting the liquid (red) within a groove coming in contact with the bottom boundary due to the large contact angle that results from a high pressure difference across the interface and the gas pocket (blue) separating. Velocity vectors are also shown.

Failure of Superhydrophobic Effect

Failure can occur because the interface contacts the side or bottom walls. The Young-Laplace equation shows that the contact angle θ is 180^o, when

$$\Delta p_{\mathrm{cr}} = 2\sigma/w. \tag{15}$$

Assuming this pressure difference to be a result of the pressure fluctuation induced by the boundary layer, we can assume that failure occurs when $\Delta p_{cr} = K p_{\mathrm{rms}} \sim 3K\rho u_\tau^2$, where K is an empirical constant, which reflects the extent to which intense instantaneous pressure events exceed their rms values. Rearrangment yields a critical Weber number:

$$\mathrm{We}_{\mathrm{cr}} = \frac{\rho u_\tau^2 w}{\sigma} = \frac{2}{3K}. \tag{16}$$

Assuming for example $\bar{U}/U_\tau \approx 18$ for $Re_\tau = 400$ (smooth channel value), $\sigma = 7.2E^{-2}N/m$, $w = 30\mu m$ yields $\bar{U} \approx 7$m/s.

The depth of the groove can also affect failure. Figure 13 shows VOF simulations of an interface which

comes into contact with the bottom wall, yielding gas pockets which move towards the side walls and the top of the groove.

If failure is defined by the loss of drag reduction, such failure may occur even when the interface is intact. Figure 14 shows deflection of the interface prescribed by Young-Laplace equation for varying values of pressure difference. Note how the deflection increases with increasing pressure difference. As discussed in the laminar channel section, when the interface penetrates considerably into the groove, the velocity at the interface approaches the no-slip condition. The shear on the liquid therefore increases, and the drag reduction goes down.

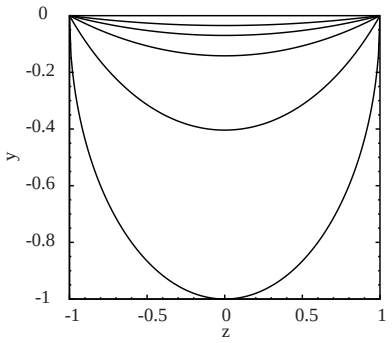

Figure 14: Plot of the meniscus interface. $\Delta p = 500, 1000, 2000, 5000, 7200$Pa, from top to bottom. Length unit is $10\mu m$. The interface penetrates into the groove as the pressure difference increases.

CONCLUSION

This paper uses direct numerical simulations to study the microphysics of superhydrophobic surfaces and their drag reducing ingredients. Good agreement is obtained with the experiments of Maynes et al. (2007). The simulation results are used to show that groove geometry, trapped gas, and interface meniscus all contribute to drag reduction. Each of these effects is independently studied. An alternative to the zero shear boundary condition is used to represent the effect of gas pocket on the outer liquid. The results show good agreement with Volume-of-Fluid simulations and analytical solution (not discussed in this paper). Turbulent simulations bounded by grooved wall on one side were performed at $Re_\tau = 400$ with groove width $w^+ = 3.6$ and height $h^+ = 3.6$. The results show that geometry causes an apparent slip to the external flow which extends up to $y^+ = 2$ from the wall and yields overall drag reduction of about 5%. The instantaneous solution shows behavior similar to riblets in that the near wall vorticity does not penetrate into the grooves yielding overall drag reduction. The failure of the interface is examined and a simple criterion is proposed.

ACKNOWLEDGMENT

This work was supported by the United States Office of Naval Research under ONR Grant N00014–12–1–0874 with Dr. Ki-Han Kim as the program manager. Computing resources were provided by the Argonne Leadership Computing Facility and the Minnesota Supercomputing Institute.

REFERENCES

Busse, A. and Sandham, N. D., "Influence of an anisotropic slip-length boundary condition on turbulent channel flow," Physics of Fluids, Vol. 24, No. 5, May 2012, pp. 055111.

Cassie, A. B. D. and Baxter, S., "Wettability of porous surfaces," Transactions of the Faraday Society, Vol. 40, 1944, pp. 546–551.

Choi, H., Moin, P., and Kim, J., "Direct numerical simulation of turbulent flow over riblets," Journal of Fluid Mechanics, Vol. 255, Oct. 1993, pp. 503–539.

Mahesh, K., Constantinescu, G., and Moin, P., "A numerical method for large-eddy simulation in complex geometries," Journal of Computational Physics, Vol. 197, No. 1, Jan. 2004, pp. 215.

Maynes, D., Jeffs, K., Woolford, B., and Webb, B. W., "Laminar flow in a microchannel with hydrophobic surface patterned microribs oriented parallel to the flow direction," Physics of Fluids, Vol. 19, No. 9, Sep. 2007, pp. 093603.

Moser, R. D., Kim, J., and Mansour, N. N., "Direct numerical simulation of turbulent channel flow up to $Re_\tau = 590$," Physics of Fluids, Vol. 11, No. 4, Apr. 1999, pp. 943–945.

Park, H., Park, H., and Kim, J., "A numerical study of the effects of superhydrophobic surface on skin-friction drag in turbulent channel flow," Physics of Fluids, Vol. 25, No. 11, Sep. 2013.

Philip, J. R., "Flows satisfying mixed no-slip and no-shear conditions," Zeitschrift für Angewandte Mathematik und Physik ZAMP, Vol. 23, No. 3, May 1972, pp. 353–372.

Philip, J. R., "Integral properties of flows satisfying mixed no-slip and no-shear conditions," Zeitschrift für Angewandte Mathematik und Physik ZAMP, Vol. 23, No. 6, Nov. 1972, pp. 960–968.

Pit, R., Hervet, H., and Léger, L., "Friction and slip of a simple liquid at a solid surface," Tribology Letters, Vol. 7, No. 2-3, Sep. 1999, pp. 147–152.

Pope, S. B., Turbulent Flows, 1st ed., Cambridge University Press, Cambridge, UK, 2000, pp. 271–278.

Rothstein, J. P., "Slip on superhydrophobic surfaces," Annual Review of Fluid Mechanics, Vol. 42, No. 1, Jan. 2010, pp. 89–109.

Sbragaglia, M. and Prosperetti, A., "A note on the effective slip properties for microchannel flows with ultrahydrophobic surfaces," Physics of Fluids, Vol. 19, No. 4, Apr. 2007.

Seo, J., Garciá-Mayoral, R., and Mani, A., "Pressure fluctuations and interfacial robustness in turbulent flows over superhydrophobic surfaces," Journal of Fluid Mechanics, Vol. 783, Dec. 2015, pp. 448–473.

Teo, C.J. and Khoo, B.C., "Flow past superhydrophobic surfaces containing longitudinal grooves: effects of interface curvature," Microfluidics and Nanofluidics, Vol. 9, No. 2-3, Aug. 2010, pp. 499–511.

Tretheway, D. C. and Meinhart, C. D., "Apparent fluid slip at hydrophobic microchannel walls," Physics of Fluids, Vol. 14, No. 3, Mar. 2002, pp. L9–L12.

Tretheway, D. C. and Meinhart, C. D., "A generating mechanism for apparent fluid slip in hydrophobic microchannels," Physics of Fluids, Vol. 16, No. 5, May 2004, pp. 1509–1515.

Ybert, C., Barentin, C., Cottin-Bizonne, C., Joseph, P., and Bocquet, L., "Achieving large slip with superhydrophobic surfaces: Scaling laws for generic geometries," Physics of Fluids, Vol. 19, No. 12, Dec. 2007, pp. 123601.